J. Fluid Mech. (2007), *vol.* 586, *pp.* 177–204.
doi:10.1017/S0022112007006842 Printed in the United Kingdom

Large-eddy simulation analysis of mechanisms for viscous losses in a turbomachinery tip-clearance flow

DONGHYUN YOU†[1], MENG WANG[2], PARVIZ MOIN[1] AND RAJAT MITTAL[3]

[1]Center for Turbulence Research, Stanford University, Stanford, CA 94305, USA

[2]Department of Aerospace and Mechanical Engineering, University of Notre Dame, Notre Dame, IN 46556, USA

[3]Department of Mechanical and Aerospace Engineering, George Washington University, Washington, DC 20052, USA

(Received 2 August 2006 and in revised form 4 April 2007)

The tip-leakage flow in a turbomachinery cascade is studied using large-eddy simulation with particular emphasis on understanding the underlying mechanisms for viscous losses in the vicinity of the tip gap. Systematic and detailed analysis of the mean flow field and turbulence statistics has been made in a linear cascade with a moving endwall. Gross features of the tip-leakage vortex, tip-separation vortices, and blade wake have been revealed by investigating their revolutionary trajectories and mean velocity fields. The tip-leakage vortex is identified by regions of significant streamwise velocity deficit and high streamwise and pitchwise vorticity magnitudes. The tip-leakage vortex and the tip-leakage jet which is generated by the pressure difference between the pressure and suction sides of the blade tip are found to produce significant mean velocity gradients along the spanwise direction, leading to the production of vorticity and turbulent kinetic energy. The velocity gradients are the major causes for viscous losses in the cascade endwall region. The present analysis suggests that the endwall viscous losses can be alleviated by changing the direction of the tip-leakage flow such that the associated spanwise derivatives of the mean streamwise and pitchwise velocity components are reduced.

1. Introduction

The radial clearance between a rotor-blade tip and casing wall in a turbomachine is indispensable for its operation. However, its existence has been a major source of unfavourable flow phenomena. Complicated vortical structures are generated by the tip-clearance flow and its interaction with the endwall boundary layer, the blade wake, and the neighbouring blade. The tip-clearance vortex often induces rotating instabilities and blockage in the flow passage which can result in severe performance loss and subsequent stall of axial compressors (Furukawa *et al.* 1998; Mailach, Lehmann & Vogeler 2001). In a transonic compressor, the interaction between passage shock and tip-clearance flow is implicated in the degradation of efficiency as well as vibrations and noise generation (Suder 1998).

† Author to whom correspondence should be addressed: dyou@stanford.edu.

These issues have motivated a number of experimental and computational investigations of the compressor tip-clearance flow, and a basic understanding has been achieved (see e.g. Inoue, Kuroumaru & Fukuhara 1986; Goto 1992; Stauter 1993; Lakshminarayana, Zaccaria & Marathe 1995; Foley & Ivey 1996; Puddu 1996). Experimental investigations of compressor rotors achieving pressure rises (defined as the pressure difference between the outlet and inlet of a compressor normalized by the dynamic pressure) of $0.4 \sim 0.5$ with tip-gap sizes of $0.4\,\% \sim 5\,\%$ chord and flow turning angles of $6^\circ \sim 16^\circ$, with or without inlet guide vanes, have shown the following global features of the tip-leakage flow: the tip-leakage vortex originates from the suction side of the blade tip, between 20 % to 50 % chord, and extends toward the pressure-side trailing edge of its neighbouring blade. As the vortex convects downstream, its size is expanded while its core is lifted away from the casing wall, and it remains clearly distinct at locations even further downstream from the trailing edge. In these experiments, the tip-leakage vortex was observed either as a streamwise velocity deficit or as a region of circulating mean crossflow. These studies also showed intense turbulent fluctuations associated with the tip-leakage vortex.

Quantitative studies of the flow through an actual compressor or pump have been difficult and limited due to safety issues and other technical problems. Alternatively, linear cascade facilities have been used to reproduce the essential features of the flow and have shown great success for situations where blade loading and centrifugal effects are small (e.g. Storer & Cumpsty 1990, 1994; Kang & Hirsch 1993*a*, *b*, 1994). Storer & Cumpsty (1990) studied the development of the leakage flow in a 5-blade linear cascade with tip gaps between 0.5 % and 4 % chord. Later, they showed using Reynolds-averaged Navier–Stokes (RANS) calculations that the loss mechanism associated with the tip-gap flow can indeed be modelled in a linear cascade (Storer & Cumpsty 1994). In their study, the mixing of flows with similar speeds but different directions in the tip-gap region was shown as the principal mechanism of loss (entropy creation).

In recent years, a series of experiments have been performed at Virginia Tech. (Muthanna & Devenport 2004; Wang & Devenport 2004; Wenger *et al.* 2004; Kuhl 2001; de la Riva 2001; Ma 2003) to make detailed measurements of the flow field in a low-speed linear compressor cascade with stationary and moving endwalls. In these experiments, mean velocity and vorticity components, turbulent kinetic energy, and frequency energy spectra were measured downstream of the cascade for tip gaps of 0.83 %, 1.65 %, and 3.3 % chord. Wang & Devenport (2004) employed a moving endwall and found noticeable differences in the mean velocity and Reynolds stress distributions from the experiments that utilized a stationary endwall (Muthanna & Devenport 2004). Kuhl (2001) and Ma (2003) examined the effects of upstream vortex pairs on the downstream tip-leakage vortex.

These experiments have provided useful information regarding the flow as well as valuable data for validating computational techniques. Shin (2001) and Khorrami *et al.* (2002) performed RANS simulations of the configuration considered by Muthanna & Devenport (2004) and showed a reasonable agreement with the experiment in the mean velocity and pressure coefficients. However, since the experimental measurements (Muthanna & Devenport 2004; Wang & Devenport 2004) were limited to the flow field beyond 1.5 chords from the trailing edge, they could not shed light on the upstream flow features which are critically important.

Experimental measurements of the tip-leakage flow in the vicinity of the tip gap very close to the moving endwall are generally difficult due to technical and safety issues. In addition, the strongly unsteady nature of the tip-leakage flow limits the applicability of conventional Reynolds-averaged Navier–Stokes (RANS) approaches

in the computational interpretation of the flow physics. These difficulties have been major obstacles to a detailed understanding of the tip-leakage flow physics leading to viscous losses. Although the gross feature of the tip-leakage vortex has been known for some time, a deeper quantitative understanding of the dynamics of the tip-leakage vortical structures and their interaction with the endwall boundary layer is needed to elucidate the viscous-loss mechanisms.

In the present study, we employ large-eddy simulation (LES) to study the tip-clearance flow in the same configuration considered by Wang & Devenport (2004) particularly in regions not studied experimentally. The objective is to gain an understanding of the underlying mechanisms for viscous losses associated with the tip-leakage flow. In order to gain such an understanding, it is necessary to study the detailed mean flow and turbulence dynamics in the vicinity of the tip-clearance region. Through a quantitative analysis of the vorticity and turbulent-kinetic-energy production mechanisms, the major sources of viscous losses in the tip-gap flow are elucidated, and means to mitigate the losses are proposed.

The paper is organized as follows. Computational details such as inflow, grid resolution, and CFL number effects are described in § 2. Details of the mean flow and turbulence dynamics and mechanisms for viscous losses associated with the tip-leakage flow are discussed in § 3, followed by conclusions in § 4.

2. Computational methodology

2.1. *Numerical method*

The numerical algorithm and solution method are described in detail in You *et al.* (2004*a*). Here, we summarize the main features of the methodology. The three-dimensional, unsteady, incompressible Navier–Stokes equations are solved in a generalized-coordinate system in conjunction with a Smagorinsky-type dynamic subgrid-scale (SGS) model. Given the fully inhomogeneous nature of the flow, a Lagrangian dynamic SGS model, which averages the model coefficient along the flow pathlines (Meneveau, Lund & Cabot 1996), is employed.

The dependent variables in the governing equations are volume fluxes across the faces of the cells, which are equivalent to using the contravariant-velocity components on a staggered grid multiplied by the Jacobian of the coordinate transformation. With this choice of variables, the discretized mass conservation can be easily satisfied. The key feature of the numerical method is the use of a non-dissipative, central-difference spatial-discretization scheme on a staggered grid, which has been demonstrated to be crucial for retaining the accuracy and predictive capability of the LES approach (You, Wang & Moin 2006*b*; Mittal & Moin 1997).

The integration method used to solve the governing equations is based on a fully implicit fractional-step method, which avoids the severe time step restriction in the tip-clearance region. All terms including cross-derivative diffusion terms are advanced in time using the Crank–Nicolson method. A Newton iterative method is used to solve the discretized nonlinear equations. For the pressure Poisson equation, an efficient multigrid procedure, which is a combination of the line and red–black Gauss–Seidel multigrid methods, is used. This method is particularly appropriate for parallelization. The simulation code is parallelized using OpenMP.

2.2. *Flow configuration*

The flow configuration and the coordinate definition are schematically shown in figure 1. The presence of the tip clearance between the rotor tip and the endwall poses a considerable challenge for the grid topology and resolution, and this factor

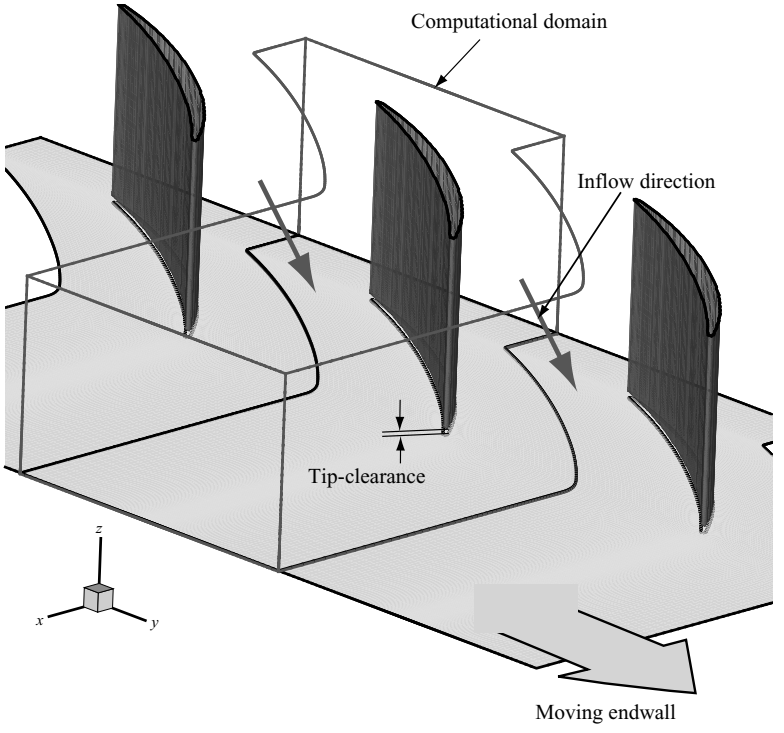

FIGURE 1. Flow configuration and coordinate system for tip-clearance flow.

has been a major obstacle to the accurate prediction of this flow. Commonly used mesh topologies are the multi-zone mesh, which combines H- and O-type meshes (e.g. Hoeger, Fritsch & Bauer 1999; Ameri, Steinthorsson & Rigby 1999; Khorrami, Li & Choudhan 2002), and the embedded H-type mesh (e.g. Kunz, Lakshminarayana & Basson 1993). However, the zonal mesh and the embedded H-mesh have significant drawbacks for use in LES. This is because the interpolation procedures in multi-zone meshes and the convergence of the longitudinal grid lines in the leading- and trailing-edge regions in embedded H-type meshes lead to high-aspect and stretching ratios, which are inappropriate for non-dissipative, energy-conservative numerical schemes (You *et al.* 2006*a*).

To overcome the above difficulty, a novel approach, which combines the immersed-boundary technique with a structured grid in generalized curvilinear coordinates, is employed to treat the tip-gap region (You *et al.* 2004*a*). The immersed-boundary method, when used with the curvilinear mesh, obviates a complex mesh topology and allows the use of a simple single-block mesh. The key advantage of using a curvilinear mesh is that it can ensure adequate resolution of the boundary layers with a much smaller mesh size than that required when a Cartesian mesh is employed as in the conventional immersed-boundary method (e.g. Fadlun *et al.* 2000).

The present study is focused on a linear cascade with a moving endwall at the bottom of the tip gap that matches the experimental setup of Wang & Devenport (2004). In the experiments (Muthanna & Devenport 2004; Wang & Devenport 2004), the linear cascade was designed to avoid aperiodic features of the tip-leakage flow in the pitchwise direction, and it was confirmed that the tip-leakage flow is periodic in the pitchwise direction in terms of velocity, pressure, and blade loading. Therefore,

$Re\ (=U_\infty C/\nu)$	L_x	L_y (= pitch)	L_z (= span)	tip-gap size	stagger angle
4×10^5	$3.30C_a$	$1.70C_a$	$0.92C_a$	$0.03C_a$	56.9°

TABLE 1. Physical parameters used in the simulation.

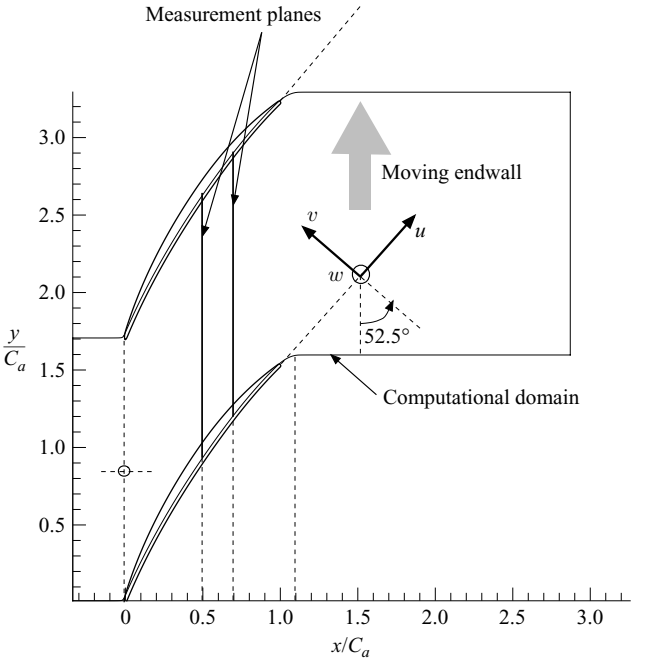

FIGURE 2. Measurement planes for investigating the flow field in the cascade and definitions of velocity coordinates.

a single-blade passage is considered in the present study, with periodic boundary conditions in the y-direction to mimic the flow in the interior of a cascade. The computational domain is of size $L_x\times L_y\times L_z = 3.30C_a\times 1.70C_a\times 0.92C_a$, where C_a is the blade axial chord and x, y, and z denote streamwise, pitchwise, and spanwise coordinates, respectively.

The important parameters for the simulation are as follows: the size of the tip clearance is $0.03C_a$, the blade pitch is $1.70C_a$, and the blade span is $0.92C_a$. The blade has a relatively high stagger-angle of 56.9 degrees. The Reynolds number of this flow is 400 000 based on the chord (C) and the inflow free-stream velocity (U_∞). The coordinate variables are normalized using the blade axial chord C_a ($=0.546C$). The physical parameters used in the present simulation are summarized in table 1.

In the present study, an extensive analysis of the mean flow and turbulence statistics is made in a number of x–y planes parallel to the endwall and y–z planes perpendicular to both the endwall and the streamwise direction, as shown in figure 2. The velocity coordinates are also shown in figure 2, where u, v, and w refer to the streamwise, pitchwise, and spanwise velocity components, respectively. In the present study, each velocity component is decomposed as:

$$u = U + u', \quad v = V + v', \quad w = W + w', \tag{2.1}$$

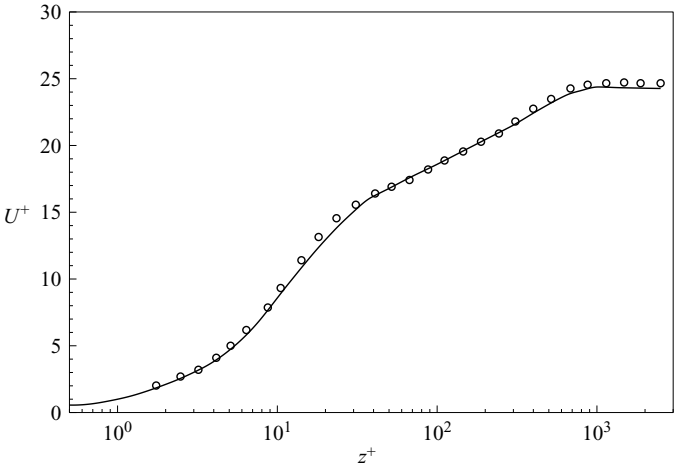

FIGURE 3. Mean streamwise velocity in the inflow turbulent boundary layer in wall units at $Re_\theta = 780$. ——, LES; ○, Kuhl (2001) at $Re_\theta = 703$.

where U, V, and W represent the time-averaged streamwise, pitchwise, and spanwise velocity components, respectively, and u', v', and w' are the corresponding fluctuating components.

No-slip boundary conditions are applied along the rotor blade and moving endwall, while inviscid-flow boundary conditions are imposed on the stationary top boundary:

$$\frac{\partial u}{\partial z} = \frac{\partial v}{\partial z} = w = 0 \quad \text{at } z = 0.92C_a. \tag{2.2}$$

The inflow turbulent boundary layer, at Reynolds number of 780 based on the momentum thickness, is generated by a separate LES of a turbulent boundary layer on a stationary flat plate using the method of Lund, Wu & Squires (1998), modified to accommodate the pitchwise non-zero mean velocity due to the skewness angle of the inflow. Figure 3 shows the inflow velocity profile which agrees reasonably well with the experimental data of Kuhl (2001) measured in the same wind tunnel facility of Wang & Devenport (2004). At the inlet of the computational domain where the bottom endwall is stationary, the endwall boundary layer thickness is 9.4 % of the spanwise domain size (L_z) and the spanwise domain size in wall units (L_z^+) is about 8200.

In figures 4(a) and 4(b), the mean streamwise velocity and the intensity of streamwise velocity fluctuations obtained from the LES are compared with the experiment of Wang & Devenport (2004) at the location ($x/C_a = 0$, $y/C_a = 0.85$) shown in figure 2, which is a short distance from the inlet. To satisfy the no-slip condition on the moving endwall, the speed of which is 90.8 % of the inflow free-stream velocity, the streamwise velocity on the endwall is non-zero ($\mathscr{U}_{\text{endwall}}/U_\infty = 0.908 \sin(52.5^\circ) = 0.72$). Except for the region very close to the endwall, the comparisons are reasonable considering the experimental difficulty of measuring velocities very near the moving endwall.

The convective boundary condition

$$\frac{\partial u_i}{\partial t} + U_c \frac{\partial u_i}{\partial x_1} = 0 \tag{2.3}$$

Inlet	Outlet	y-direction	Top wall	Bottom wall	Blade
turbulent boundary layer	convective	periodic	inviscid	no-slip	no-slip

TABLE 2. Boundary conditions used in the simulation.

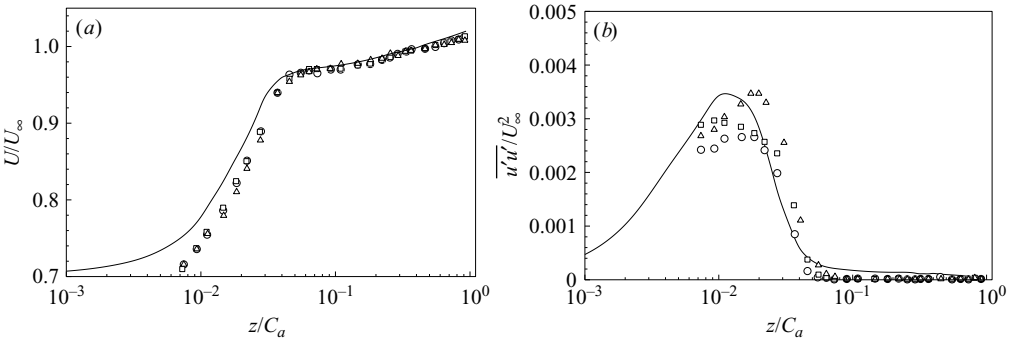

FIGURE 4. Profiles of (a) the mean streamwise velocity and (b) the mean streamwise Reynolds stress at $x/C_a = 0$ and $y/C_a = 0.85$. ———, present LES; ○, □, △, experiment (Wang & Devenport 2004). Different symbols represent different measurement locations in the 7-blade cascade.

is applied at the exit boundary, where the convection speed U_c is set equal to the mean streamwise velocity integrated across the exit plane. The boundary conditions used in the present simulation are summarized in table 2.

2.3. *Spatial and temporal resolution*

The mesh size used for the present simulation is $449 \times 351 \times 129$ ($x \times y \times z$). Curvilinear meshes are employed in the x–y plane and a non-uniform Cartesian mesh is used in the z-direction. Grid lines are clustered around the tip gap, blade surfaces, and the endwall to ensure appropriate resolution in important flow regions. A total of 36 mesh points are allocated across the tip-gap region. The grid stretching ratio is less than 2 % in the streamwise direction. The grid skewness effects on the solution have been extensively discussed in You *et al.* (2006*a*). In this study, it was shown that additional introduction of dissipation and dispersion errors is not significant for the present mesh skewness. Furthermore, it has been shown that the mesh skewness does not alter the order of accuracy of the scheme.

The grid spacing and resolution in wall units in the important regions are reported in You *et al.* (2004*b*) in detail. In general, the grid resolution on the blade surface is reasonable compared to previous LES studies of wall-bounded turbulent flows using similar numerical methods (Akselvoll & Moin 1995). In wall units, the blade surface resolution in the region of primary interest is within the range $\Delta x^+ \leqslant 50$, $\Delta y^+ \leqslant 3$, and $\Delta z^+ \leqslant 30$ (Δz^+ increases up to 90 far from the tip-gap region). The endwall boundary layer is reasonably well resolved. Grid resolution normal to the endwall is in the range of $0.3 \leqslant \Delta z^+ \leqslant 2.1$. The maximum Δz^+ is found underneath the blade tip. Near the leading edge, the endwall boundary layer thickness is about $4.8\,\%L_z$ and larger than the tip-gap size ($3.28\,\%L_z$). The tip-gap size at the tip leading-edge location is roughly 19 local wall units. The endwall motion reduces the bottom-wall shear stress and results in a smaller spanwise domain size in wall units ($L_z^+ \approx 597$) than that measured at the inlet of the computational domain ($L_z^+ \approx 8200$) where the

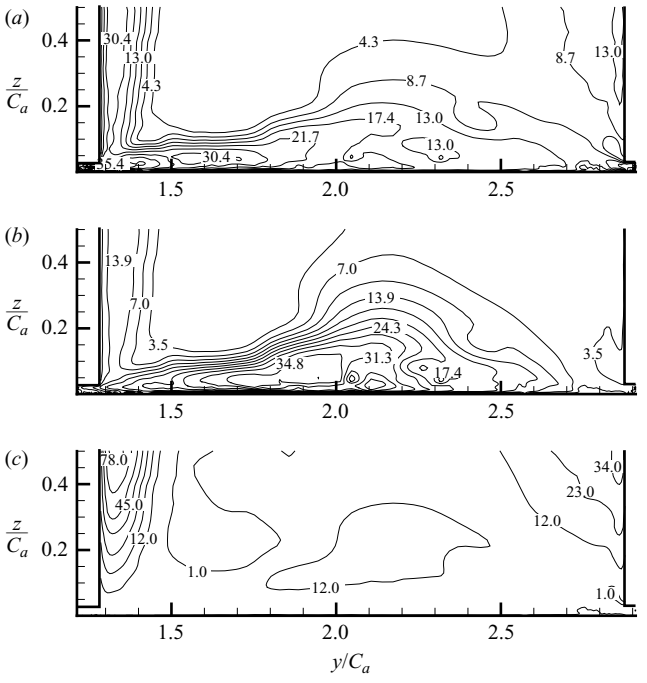

FIGURE 5. Resolution in Kolmogorov units (η) in a y–z plane at $x/C_a = 0.7$. (*a*) $\Delta x/\eta$; (*b*) $\Delta y/\eta$; (*c*) $\Delta z/\eta$.

bottom endwall is stationary. In the directions parallel to the endwall, Δx^+ and Δy^+ are generally less than 50.

The resolution in Kolmogorov units (η), which is estimated by an evaluation of the production and assuming equilibrium, is in the range of $\Delta x/\eta, \Delta y/\eta \leqslant 40$, and $\Delta z/\eta \leqslant 10$ in the endwall region, while $\Delta z/\eta$ increases up to 110 far from the endwall. Figure 5 shows that ratios of the grid spacing to the Kolmogorov length scale in the endwall parallel directions are relatively high underneath the blade tip and around the tip-leakage-vortex core (figures 5*a* and 5*b*), while the ratio of the spanwise grid spacing to the Kolmogorov length scale is relatively high on the suction surface boundary layer far from the endwall (figure 5*c*). The present LES is found capable of predicting the broadband characteristics of the turbulent fluctuations present in the endwall tip-leakage flow. For example, figure 6 shows the streamwise velocity energy spectrum computed in the core of the tip-leakage vortex at $x/C_a = 1.51$. The velocity energy spectrum is in favourable agreement with the experimental data provided by Wang & Devenport (2004) and shows an inertial subrange which is typically described with the slope of $-5/3$.

The flow field near the suction surface necessitates enhanced eddy viscosity compared to the pressure side where the eddy viscosity becomes negligible because of the very low level of turbulence activity. Except for the relatively coarse mesh region in the blade wake far from the endwall, the peak eddy viscosity is usually less than 7 times the value of the molecular viscosity, which is similar to the magnitude observed in the successful LES study of backward-facing-step flow (Akselvoll & Moin 1995). Figure 7 shows the resolved and total Reynolds shear-stress profiles along the spanwise direction at $x/C_a = 0.6$ and $y/C_a = 1.51$. It apparently indicates that the contribution of the subgrid-scale shear stress to the total Reynolds shear stress is reasonably small.

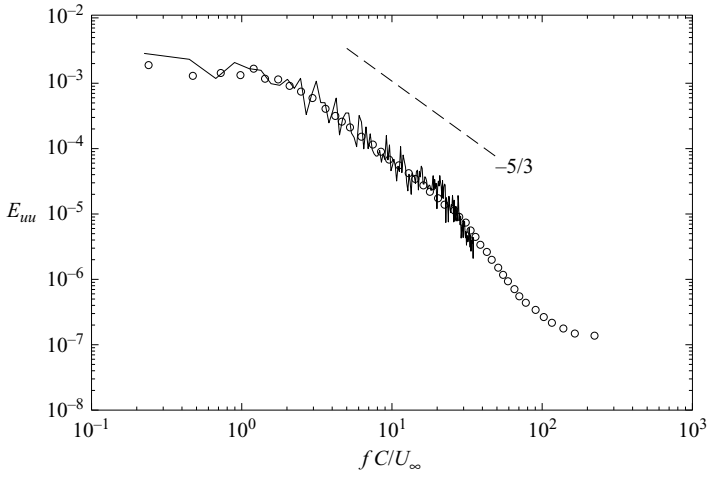

FIGURE 6. Streamwise velocity energy spectra as a function of frequency in the core of the tip-leakage vortex at $x/C_a = 1.51$. ———, present LES; ○, experiment (Wang & Devenport 2004).

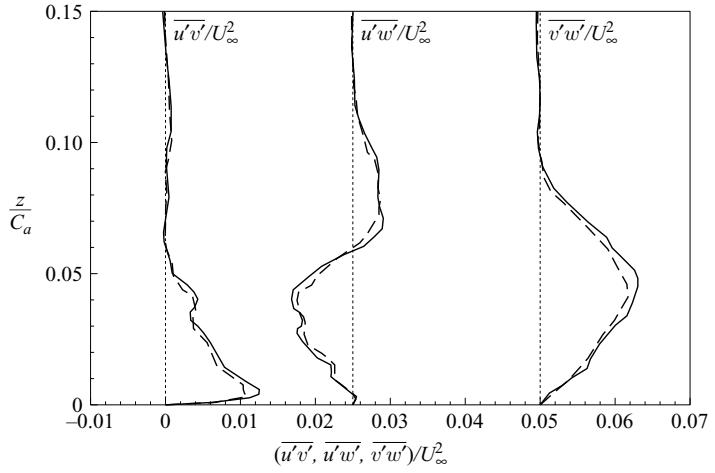

FIGURE 7. Profiles of Reynolds shear stresses along the spanwise direction at $(x/C_a, y/C_a) = (0.6, 1.51)$. ———, total stress; – – – –, resolved stress. The profiles of $\overline{u'w'}/U_\infty^2$ and $\overline{v'w'}/U_\infty^2$ are shifted by 0.025 and 0.05, respectively.

Prior to this simulation, coarser grid simulations had been carried out to determine the resolution requirements, and the final mesh was subsequently constructed using this information. To investigate the grid sensitivity, simulations of flow through the cascade without a tip gap, which are less expensive than the present simulation, were performed with refined meshes in all three directions, and it was confirmed that results are relatively insensitive to the grid resolution. The grid resolution study and a systematic validation of the LES predictions were reported in You *et al.* (2004*a*,*b*). Qualitative and quantitative agreements with experiments (Wang & Devenport 2004) in terms of mean velocity, Reynolds stresses, and energy spectra have been obtained in the downstream measurement planes. The present numerical scheme has been found to be good in predicting the turbulence energies in a wide frequency range without excessive numerical dissipation.

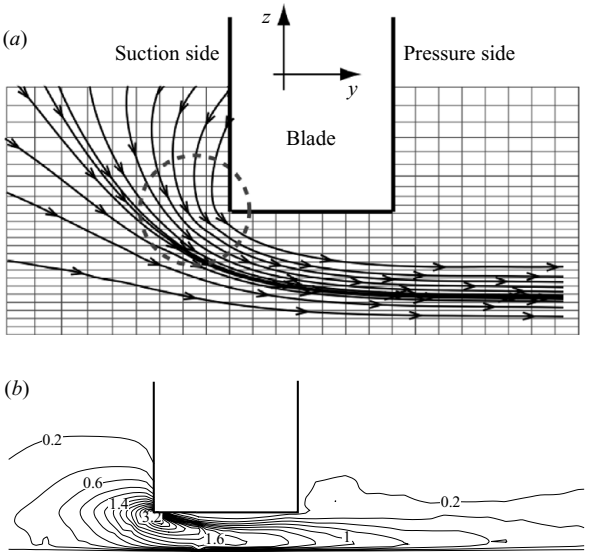

FIGURE 8. (*a*) Mean streamlines and (*b*) contour plot of CFL number distribution in a y–z plane at $x/C_a = 0.7$. In (*a*), every third and second points are shown in y- and z-directions, respectively.

The simulation is advanced in time with the maximum convective Courant–Friedrichs–Lewy (CFL) number equal to 4, which corresponds to $\Delta t U_\infty / C \approx 0.73 \times 10^{-3}$, where U_∞ is the incoming free-stream velocity. Each time step requires a wall-clock time of about 200 seconds when 128 CPUs of an SGI Origin 3800 are used.

The effect of CFL number on the instantaneous solution has been examined in simulations performed with CFL numbers of 1.5, 2.5, 4 and 5. In terms of the amplitude and phase, the variations of streamwise velocity are reasonably robust up to a CFL number of 4. The convergence property of the Newton iteration method, which is employed for solving a set of nonlinear equations, also limits the maximum allowable CFL number. In general, the number of iterations for obtaining a required convergence increases with the CFL number. For example, $6 \sim 7$ iterations are required when a CFL number of 4 is employed, while convergence is sometimes never achieved for higher CFL numbers.

The maximum CFL number occurs near the pressure side of the blade tip, where the strong downward flow passes across the dense mesh region aligned parallel to the blade tip and to the blade surface, as seen in figure 8, and except for this location, the CFL number is much less than 1. The severe time step restriction in the dense mesh region is avoided by employing a fully implicit integration method. In wall units, the time step (Δt^+) is generally far less than 0.8. The results, which will be discussed below, are obtained by integrating the governing equations over a time interval of about $30C/U_\infty$.

3. Results and discussion

3.1. *Overall features of the flow field*

Gross features of the endwall vortical structures found in the present study are illustrated in figure 9. The predominant vortical structure is the tip-leakage vortex, which is formed due to roll-up of the tip-leakage jet and originates at about 20 % to

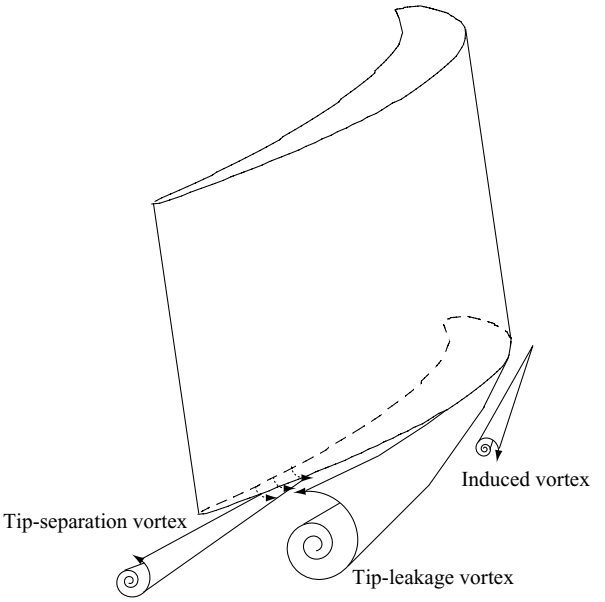

FIGURE 9. Illustration of the flow structures found in the cascade endwall region.

30 % of the axial chord downstream from the leading edge. The tip-leakage vortex also generates induced vortices in the upstream positive pitchwise locations. The tip-separation vortices are formed due to flow separation underneath the blade tip. The endwall vortical structures are also visualized using the λ_2 vortex-identification method (Jeong & Hussain 1995) and shown in figure 10. In the vicinity of the tip gap, the blade boundary layer transition is naturally triggered by the interaction with the endwall turbulent boundary layer. In the downstream locations from the trailing edge, the endwall vortical structures become highly complicated due to the interaction of the tip-leakage vortex, tip-separation vortices, and blade wake. In parallel with the present study, You *et al.* (2005) performed a detailed analysis of the vortex-shedding frequency in the blade wake and the space–time correlations of the velocity fluctuations in the endwall tip-leakage flow, and suggested that the tip-leakage vortex is subject to a pitchwise low-frequency wandering motion. Similar observations have been reported by other experimental and numerical studies in tip-clearance configurations (Zierke & Straka 1996; Muthanna & Devenport 2004; Wang & Devenport 2004).

Trajectories of the tip-leakage vortex, the trailing-edge tip-separation vortex, and the blade wake are compared in figure 11 with experimental measurements (Wang & Devenport 2004; Muthanna & Devenport 2004). The core of the tip-leakage vortex is defined as the point of maximum streamwise vorticity through the tip-leakage vortex similar to that in the experiment (Wang & Devenport 2004). The trailing-edge tip-separation vortex is found using the λ_2 vortex-identification method and the core of the λ_2 contour is used to determine its trajectory. To describe the trajectory of the blade wake, locations of peak streamwise velocity deficits at $z/C_a = 0.9$ are traced. Far from the endwall, the blade boundary layer transition occurs after the separation near the trailing edge.

The trajectories of the tip-leakage vortex and blade wake are in good agreement with experimental data. Details regarding the tip-separation vortices were not documented in the experimental study. In particular, the spatial resolution of their measurements

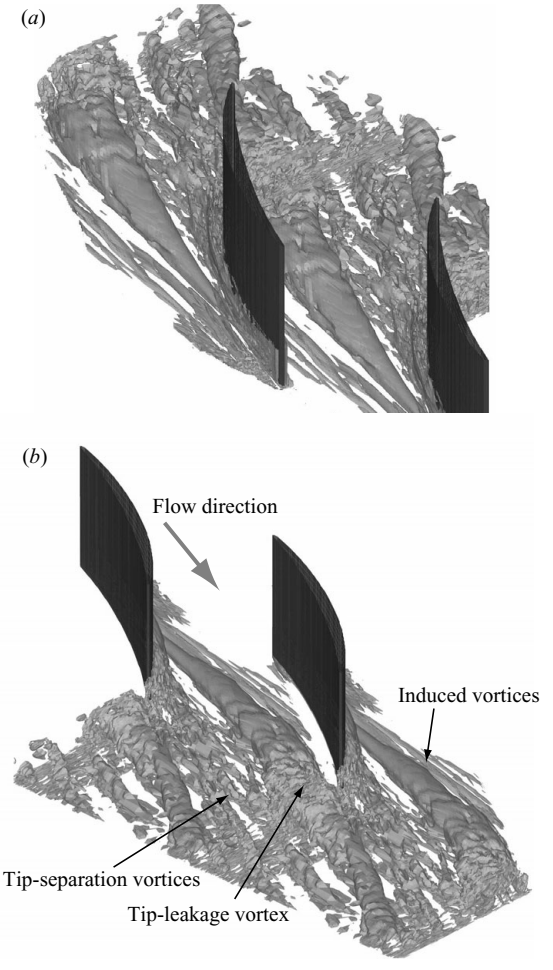

FIGURE 10. λ_2 iso-surfaces from time-averaged flow field. (*a*) Downstream view; (*b*) upstream view.

is insufficient to resolve the endwall vortical structures. The trajectories of the tip-leakage vortex in the cascade passage region ($x/C_a \leqslant 1$) and tip-separation vortex downstream of the trailing edge show larger propagation angles with the streamwise coordinate compared to those found in the rest of the tip-leakage vortex and the blade wake. Since the tip-leakage vortex in the cascade passage and the downstream tip-separation vortices are close to the endwall, their locations are strongly affected by the endwall motion in the positive pitchwise direction. Downstream of the trailing edge, the tip-leakage vortex is lifted from the endwall. Its trajectory and the trajectory of the blade wake are hence aligned with the main stream of the cascade.

Figure 12 shows the variation of the height of the tip-leakage vortex centre in terms of the maximum streamwise vorticity magnitude along the streamwise direction. In the blade passage, the height increases rapidly and nearly linearly with the streamwise coordinate, while its slope is much reduced as the tip-leakage vortex convects downstream from the trailing edge. The vortex-core locations predicted in the present study are comparable with the available experimental data at two downstream locations, $x/C_a = 1.51$ and 2.74.

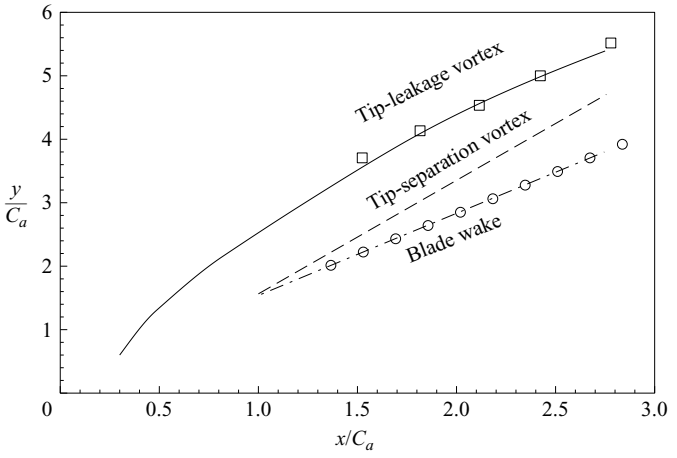

FIGURE 11. Trajectories of tip-leakage-vortex core, the trailing-edge tip-separation vortex and the centre of blade wake along the streamwise direction. ———, – – – –, —·—, present LES; □, ○, experiment (Wang & Devenport 2004).

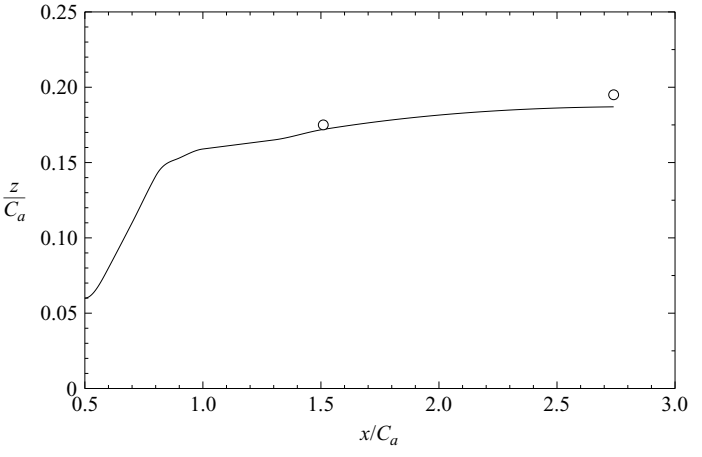

FIGURE 12. Variation of the height of the tip-leakage-vortex centre from the endwall along the streamwise direction. ———, present LES; ○, experiment (Wang & Devenport 2004).

To examine the quantitative features of the tip-leakage flow, contour plots of mean velocity components, in a number of $x-y$ planes along the blade span, are shown in figures 13–15. In the plane at $z/C_a = 0.01$ (figure 13), which is very close to the endwall, it is found that a significant blockage to the endwall passage flow is developed in the region of high streamwise velocity deficit which is noticeable along the line connecting the trailing edges of the neighbouring two blades (figure 13*a*). In addition, steep variations of the mean streamwise velocity are found along the locus of the tip-leakage vortex. The pitchwise velocity component attains its peak underneath the blade tip and around the tip-leakage vortex (figure 13*b*). In the spanwise velocity contours, the tip-leakage vortex and induced vortex are identified as the upward (solid contour lines) and downward (dashed contour lines) flow motions (figure 13*c*).

In the endwall parallel plane at $z/C_a = 0.1$ (figure 14), the streamwise velocity deficit is mainly found along the tip-leakage vortex and blade wake (figure 14*a*). In contrast

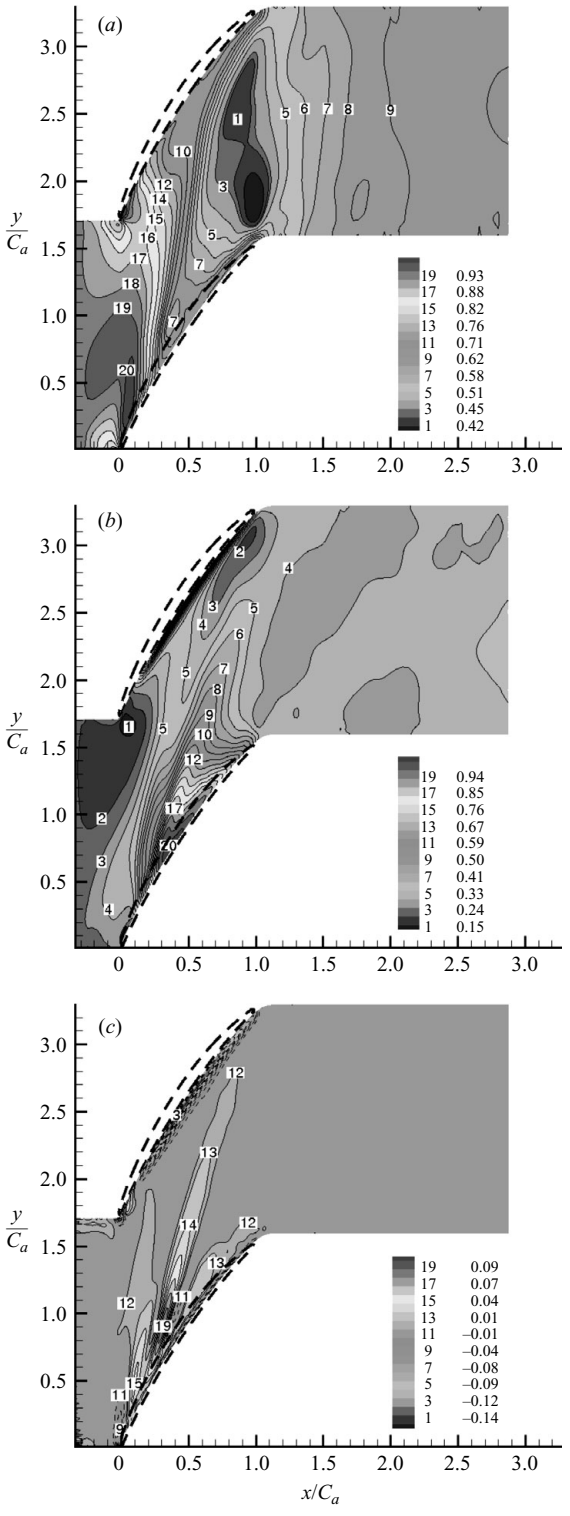

FIGURE 13. Contour plots of mean velocity components in an x–y plane at $z/C_a = 0.01$. (*a*) U/U_∞; (*b*) V/U_∞; (*c*) W/U_∞. The blade profiles (dashed lines) are shown to illustrate the locations of the blades away from the endwall.

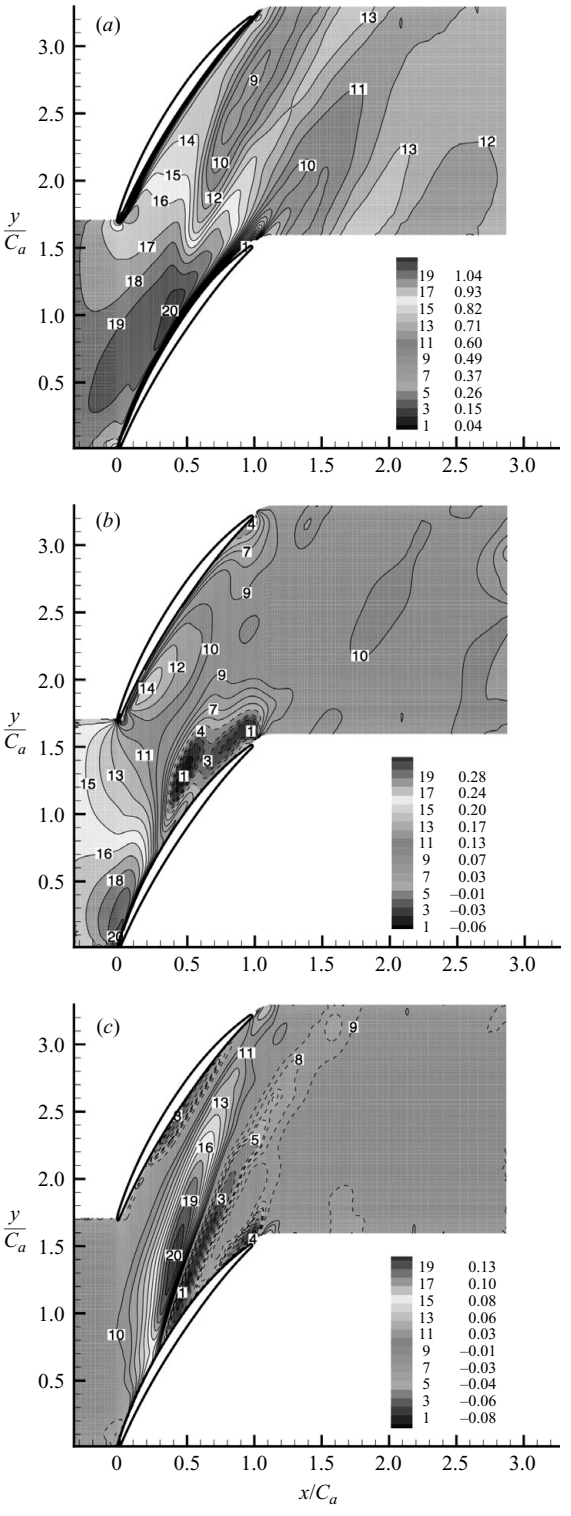

FIGURE 14. Contour plots of mean velocity components in an x–y plane at $z/C_a = 0.1$. (*a*) U/U_∞; (*b*) V/U_∞; (*c*) W/U_∞.

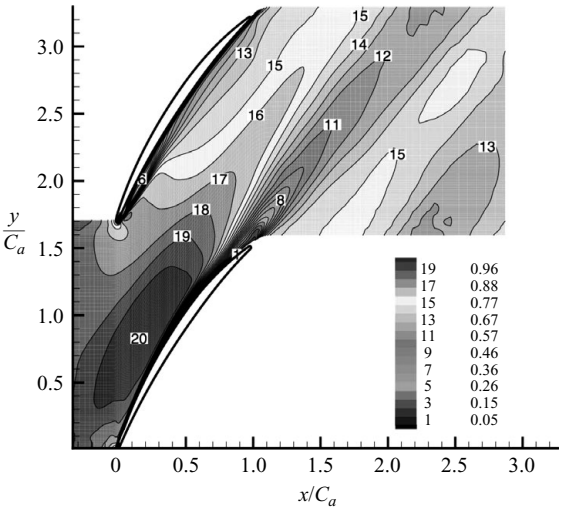

FIGURE 15. Contour plots of mean streamwise velocity in an x–y plane at $z/C_a = 0.5$.

to the mean pitchwise velocity distribution at $z/C_a = 0.01$ as shown in figure 13(b), a region of negative velocity is found near the suction surface. This combination of negative pitchwise velocity (figure 14b) and spanwise velocity (figure 14c) showing upward and downward flow motions indicates a circulating tip-leakage vortex. The influence of the tip-leakage vortex is found to be limited to about one-quarter of the axial chord from the endwall. Far from the endwall, the cascade passage flow is observed as shown in figure 15 and its variation along the span is found negligible.

3.2. *Tip-leakage jet*

The pressure difference between the pressure and suction sides of the blade tip and the moving endwall drive the tip-leakage jet across the tip gap. Although an accurate prediction of the flow field underneath the blade tip is crucial for understanding the vortical structures and their generation and evolution mechanisms, in previous studies, numerical prediction of these flow features has been difficult due to the issues of grid topology and grid resolution in the tip-gap region. Oil- or paint-film visualization techniques have been the most common way of experimentally investigating the flow field inside the tip gap.

Figure 16 shows that the endwall boundary layer near the blade tip is significantly affected by the tip-leakage jet. Near the suction side of the blade tip, the tip-leakage jet produces negative and positive mean shear stresses in the u- and v-directions, respectively (see figure 2 for the definition of the velocity coordinates). In general, high magnitudes of the shear stresses are found underneath the blade tip and near the suction side of the blade tip.

The streamlines in x–y planes away from the endwall ($z/C_a = 0.5$) and close to the endwall ($z/C_a = 0.025$) are shown in figures 17(a) and 17(b), respectively. The streamlines in the x–y plane at $z/C_a = 0.5$ (figure 17a) are mostly aligned with the blade. On the other hand, a convergence of the streamlines along the locus of the tip-leakage vortex is observed in the x–y plane close to the endwall (figure 17b). The tip-gap flow experiences a sudden change of flow direction across the converging streamlines. Upstream of the converging streamlines, the flow direction is approximately aligned with the blade chord, while the flow direction is altered to the positive pitchwise

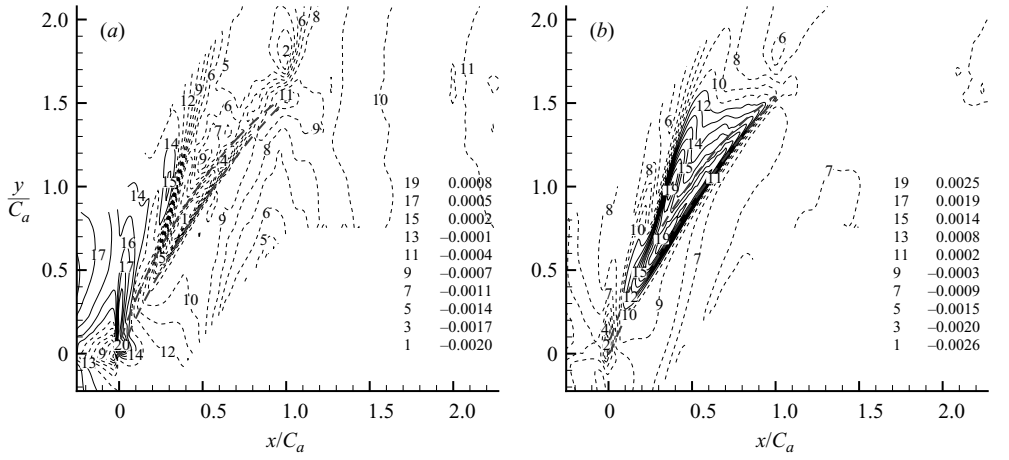

FIGURE 16. Contour plots of mean shear-stress components in an x–y plane at $z/C_a = 0$. (a) $(1/Re)(\partial U/\partial z)/U_\infty^2$; ($b$) $(1/Re)(\partial V/\partial z)/U_\infty^2$.

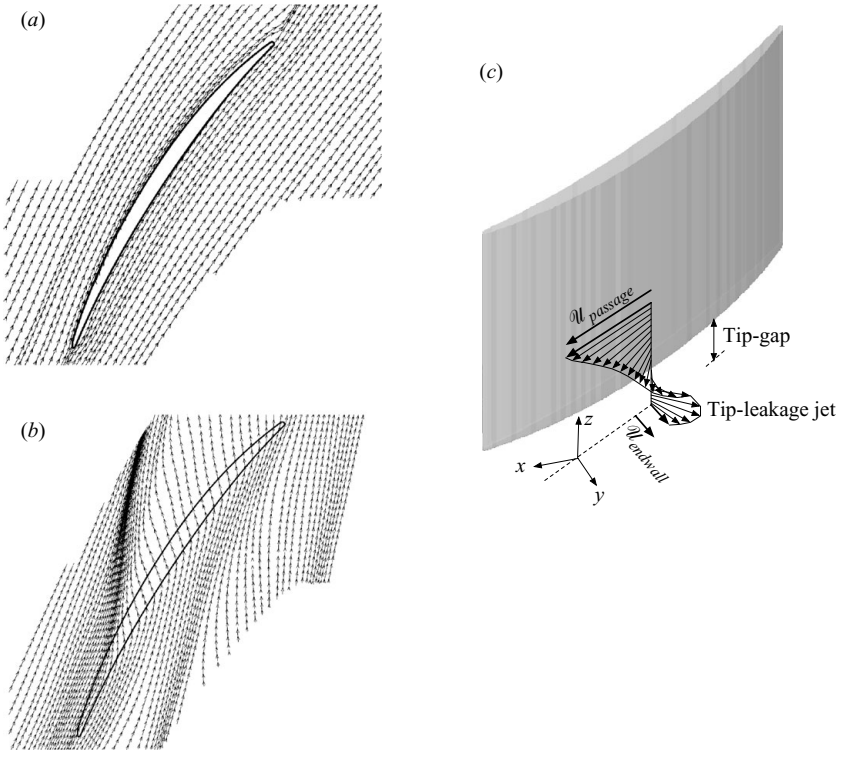

FIGURE 17. Streamlines of mean velocity field in x–y planes at (a) $z/C_a = 0.5$ and (b) $z/C_a = 0.025$, and (c) an illustration of the spanwise variation of the mean velocity.

direction in the region between the tip-leakage vortex and the blade suction surface. As a result of flow turning, the magnitude of the streamwise velocity is significantly reduced in this region, as shown in figure 13(a). The abrupt change of the streamlines along the blade span, as also shown in figures 17(a) and 17(b), results in significant spanwise derivatives of the mean streamwise and pitchwise velocity components

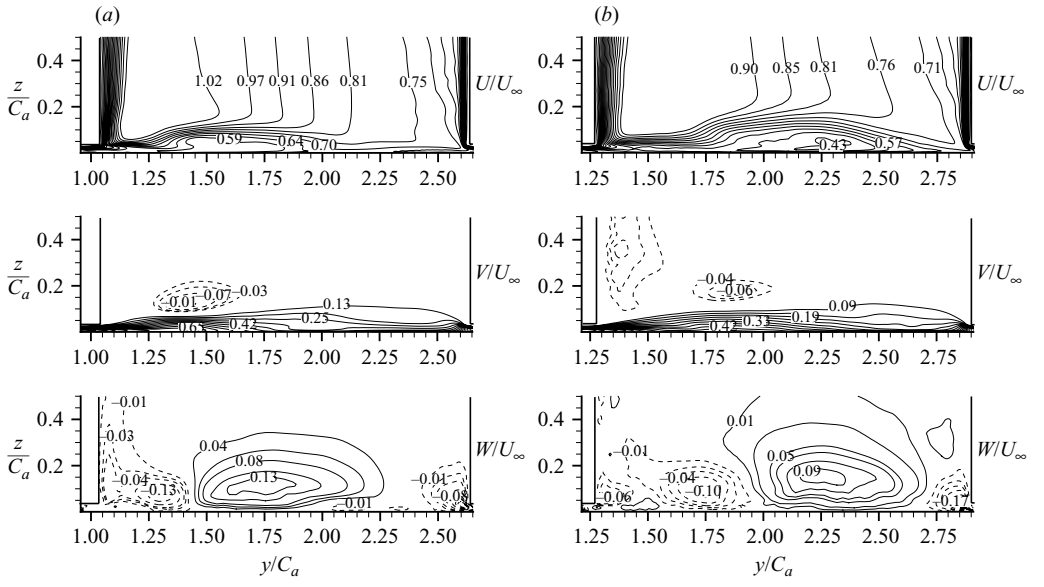

FIGURE 18. Contour plots of mean velocity components in y–z planes. (a) $x/C_a = 0.5$; (b) $x/C_a = 0.7$.

($\partial U/\partial z$ and $\partial V/\partial z$), as schematically shown in figure 17(c). As will be discussed in the following section, the large spanwise derivatives of the streamwise and pitchwise velocity components play the key role in producing the strong vorticity and turbulent kinetic energy.

3.3. *Flow field in the cascade passage*

In this section, the mean flow field and turbulence statistics in the cascade passage, where the tip-leakage vortical structures are generated and evolve, are discussed.

3.3.1. *Mean velocity field*

Figure 18 shows mean velocity components in two y–z planes from the view-point of an observer looking upstream (see figure 2 for the locations of measurement planes). The planes at $x/C_a = 0.5$ and 0.7 are found to be the most descriptive in discussing the tip-clearance flow in the cascade passage. The left-hand and right-hand sidewalls represent the suction and pressure surfaces of two neighbouring blades, respectively.

In the mid-chord location ($x/C_a = 0.5$, figure 18a), the tip-leakage vortex forms a noticeable mean streamwise velocity (U) deficit, and the location and size of the tip-leakage vortex are also clearly visualized in the mean cross-stream velocity (V and W) contours. In addition, in the spanwise velocity contour, a weak induced vortex is also observed on the lower right side of the tip-leakage vortex.

The tip-leakage vortex approaches the pressure side of the neighbouring blade with increased axial chord ($x/C_a = 0.7$, figure 18b). As the flow passes through the cascade passage, it is observed that the magnitudes of the streamwise velocity in the cascade core region and the pitchwise velocity near the endwall are rapidly reduced. This is a desired transition of dynamic head to static-pressure rise in axial compressors or pumps. The magnitude of the spanwise velocity is significantly smaller than those of the streamwise and pitchwise velocity components.

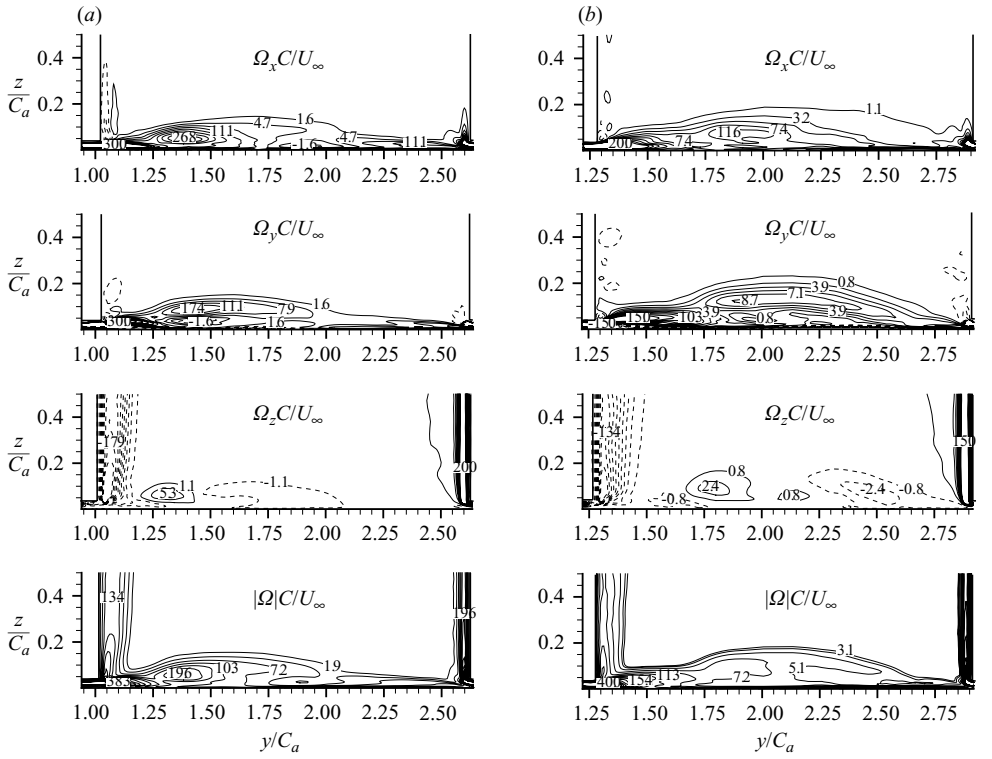

FIGURE 19. Contour plots of mean vorticity components and vorticity magnitude in y–z planes. (*a*) $x/C_a = 0.5$; (*b*) $x/C_a = 0.7$.

3.3.2. *Mean vorticity field*

The tip-leakage vortex is also often identified as the region of high vorticity magnitude. Figures 19(*a*) and 19(*b*) show the contour plots of the mean vorticity components and vorticity magnitude in y–z planes at two different streamwise locations ($x/C_a = 0.5$ and 0.7). In the endwall region, the streamwise ($\Omega_x C/U_\infty$) and pitchwise ($\Omega_y C/U_\infty$) vorticity components dominate the vorticity field, and this suggests that the tip-leakage vortex evolves in a helical configuration. The tip-leakage jet through the blade tip produces higher vorticity levels in the streamwise and pitchwise components compared to that in the tip-leakage vortex.

Streamwise vorticity in the tip-leakage-vortex core is a footprint of the cross-stream velocity field ($\Omega_x = 1/2(\partial W/\partial y - \partial V/\partial z)$) shown in figures 18(*a*) and 18(*b*), while it is mainly produced by the spanwise derivatives of the pitchwise velocity ($\Omega_x \approx -1/2\partial V/\partial z > 0$) in the tip-leakage jet. A region of high pitchwise vorticity is found between the tip-leakage vortex and the suction side of the blade tip (figures 19*a* and 19*b*). Intensive negative pitchwise vorticity is found along the jet-like leakage flow near the endwall, and this is closely related to the direction of tip-leakage flow. As shown in figure 17, the endwall leakage flow, which is directed upstream by the pressure difference between the two sides of the blade tip and the endwall motion along the positive pitchwise direction, generates strong negative pitchwise vorticity ($\Omega_y = 1/2(\partial U/\partial z - \partial W/\partial x) \approx 1/2\partial U/\partial z < 0$). On the contrary, significant levels of positive pitchwise vorticity are produced in the adjacent upper region where the leakage flow and cascade core flow generate large positive spanwise derivatives of the streamwise velocity ($\partial U/\partial z > 0$).

On the pressure and suction surfaces of the blade, the spanwise vorticity ($\Omega_z C/U_\infty$) is dominant due to the boundary layer development. In general, in the blade passage, the regions of tip leakage, blade tip, and blade boundary layers generate strong vorticity magnitudes ($|\Omega|C/U_\infty$). Among them, the vorticity magnitude underneath the blade tip overwhelms the magnitudes found in the regions of the tip-leakage vortex and the blade boundary layer. In the present study, the location of the peak streamwise vorticity is defined as the tip-leakage-vortex core as in the experiment (Wang & Devenport 2004). The peak vorticity magnitude in the tip-leakage vortex decays as it develops downstream (see figures 19*a* and 19*b*). In addition, as also observed in experiments (Wang & Devenport 2004), the tip-leakage vortex further downstream from the trailing edge decays rapidly with the streamwise coordinate.

A vortex generator can be utilized to diminish the strength of the tip-leakage vortex. Kuhl (2001) and Ma (2003) examined the effects of an upstream counter-rotating vortex pair produced by a vortex generator on the tip-leakage vortex. They observed significant modification of the downstream tip-leakage flow field. However, from the perspective of the streamwise vorticity field which mainly consists of anti clockwise-rotating vortices (from the view-point of an observer looking upstream from a downstream location), it appears more desirable to employ a vortex generator which generates only clockwise rotating vortices instead of the counter-rotating vortex pair. In order to control the pitchwise vorticity, which is quite significant in the tip-leakage jet region, shape modification of the blade cross-sectional profile and blade tip seems to be more appropriate since the direction and magnitude of the pressure gradient across the blade tip is the major source of the vorticity.

3.3.3. *Reynolds stresses*

The regions of the tip-leakage jet, tip-leakage vortex, and blade boundary layer are found as the active sources of turbulent fluctuations. Figures 20(*a*) and 20(*b*) show contour plots of Reynolds stresses in y–z planes at two axial locations of $x/C_a = 0.5$ and 0.7. In the plane at 50 % axial chord (figure 20*a*), the boundary layer on the blade suction surface and tip-leakage jet generate higher magnitudes of $\overline{u'u'}$ than the tip-leakage vortex produces. However, for $\overline{v'v'}$ and $\overline{w'w'}$, the contribution of the blade boundary layer becomes much smaller than that of the tip-leakage flow. The tip-leakage jet and tip-leakage vortex also correspond to the region of intensive Reynolds shear stresses, and their gross magnitudes appear to be much smaller than those of Reynolds normal stress components. $\overline{u'v'}$ and $\overline{u'w'}$ components show sign changes across the tip-leakage vortex, while $\overline{v'w'}$ component is mostly positive.

As shown in figure 20(*b*), at the 70 % axial-chord location, most of the endwall region and the region near the blade suction surface involve high turbulent fluctuations. In particular, the region close to the suction surface blade tip, where the tip-leakage jet and tip separation occur, is observed to generate the most active turbulent fluctuations. In this plane, the region of active turbulent fluctuations extends to about 20 % axial chord in the spanwise direction from the endwall (figure 20*b*). Sign changes of $\overline{u'v'}$ are observed in the tip-leakage core region, while $\overline{u'w'}$ and $\overline{v'w'}$ components are mostly dominated by negative and positive values, respectively. Similar trends of the Reynolds stress distributions are observed at locations further downstream.

Previous experimental and numerical studies also reported the tip-leakage vortex and tip separation as the main sources of turbulent fluctuations. Puddu (1996) reported that turbulence intensities were dominated by the components parallel to

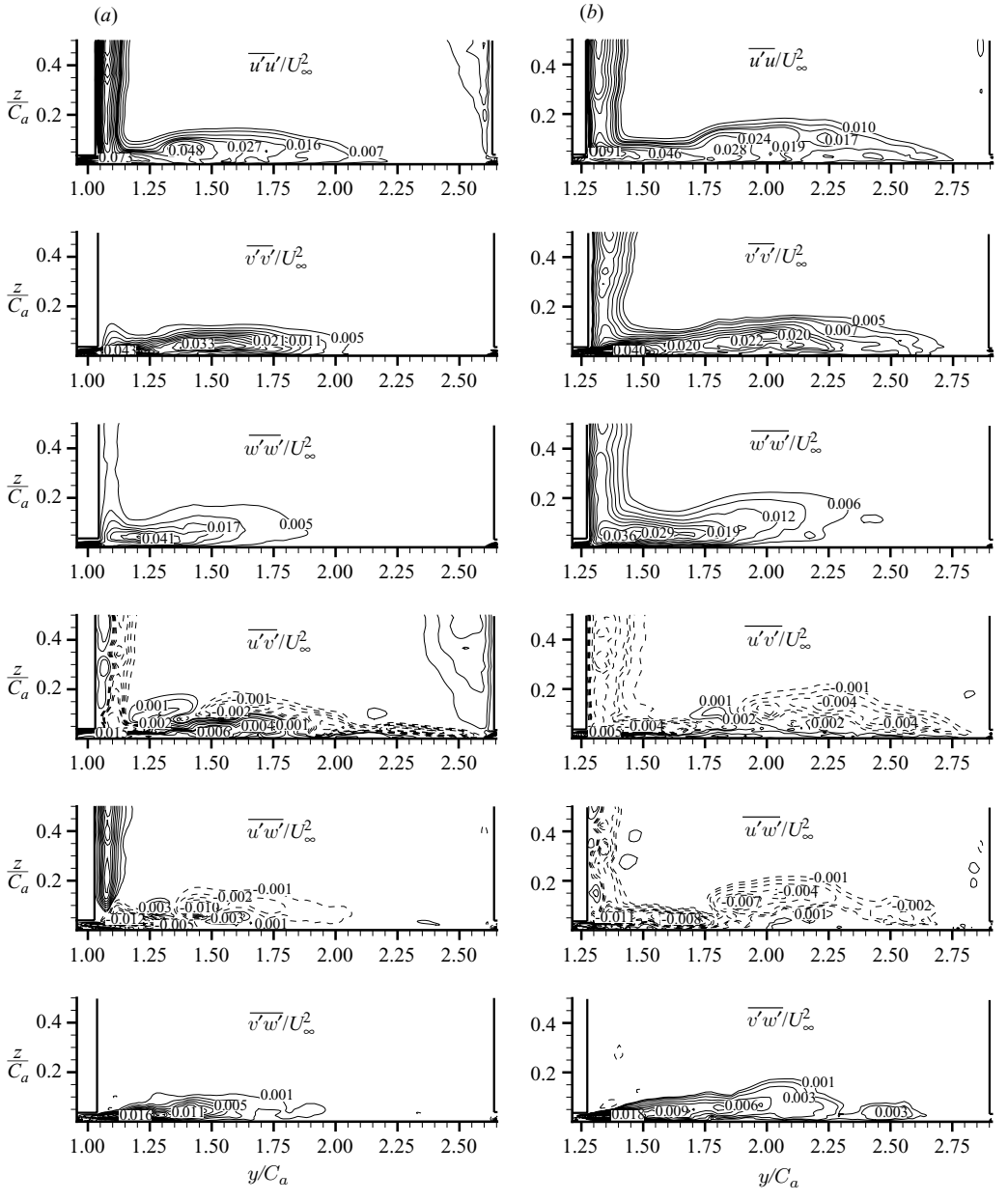

FIGURE 20. Contour plots of mean Reynolds stresses in y–z planes. (*a*) $x/C_a = 0.5$; (*b*) $x/C_a = 0.7$.

the casing. However, this is inconsistent with the findings of Lakshminarayana, Pouagare & Davino (1982) that spanwise velocity fluctuations and the Reynolds shear stresses associated with them are more significant than other components in the tip-leakage flow. The present results support the findings of Puddu (1996). As shown in figures 20(*a*) and 20(*b*), the normal-stress components $\overline{u'u'}$ and $\overline{v'v'}$ are larger than that of $\overline{w'w'}$. However, the Reynolds shear stresses $\overline{u'w'}$ and $\overline{v'w'}$, which are related to the spanwise velocity fluctuations, are comparable to $\overline{u'v'}$. The spatial distribution of

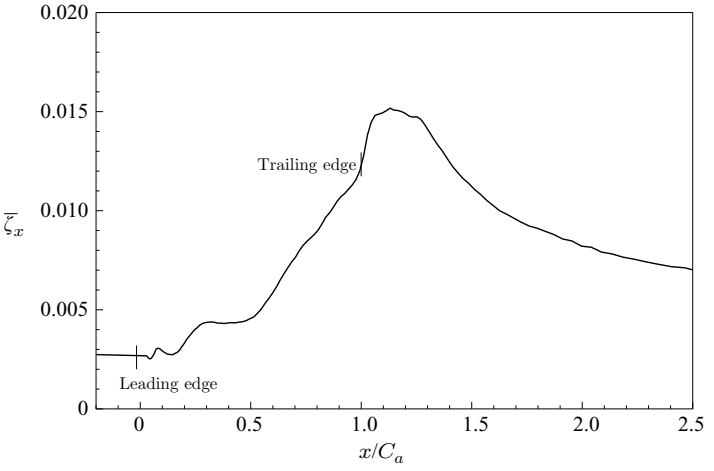

FIGURE 21. Axial development of the tip-leakage-loss coefficient ($\overline{\zeta}_x$).

each Reynolds stress component shows a highly anisotropic endwall turbulent flow field.

It has been known that the dominant source of the tip-leakage-flow loss is the interaction between the tip-leakage flow and the cascade main flow causing turbulent mixing, along with the formation and dissipation of the vortical structures (Lakshminarayana 1996). Lakshminarayana suggested that the tip-leakage loss is proportional to kinetic energy in velocity fluctuations caused by the tip-leakage flow, and proposed an approach for estimating the tip-leakage loss in favourable accuracy:

$$\text{Tip-leakage loss} \sim \overline{\zeta}_x = \frac{\text{turbulent kinetic energy caused by the tip-leakage flow}}{\text{inlet kinetic energy}} = \frac{\left\{ \int_0^{L_z^*} \int_0^{L_y} (\overline{v'^2} + \overline{w'^2}) \, \mathrm{d}y \, \mathrm{d}z \right\}_x}{U_\infty^2 L_y L_z^*}, \tag{3.1}$$

where $\overline{\zeta}_x$ is the loss coefficient due to the tip-clearance flow and L_z^* is the spanwise domain size containing the tip-leakage flow.

The present LES results are employed for evaluating the loss distribution along the streamwise direction shown in figure 21. The tip-leakage-loss coefficient increases with the streamwise direction in the cascade passage, attains its peak just downstream from the trailing edge, then decreases as the tip-leakage flow convects downstream. This trend is a reflection of the streamwise variation of the turbulence intensity and qualitatively quite similar to the experimental measurements in an axial cascade performed by Bindon (1989).

3.3.4. *Turbulent kinetic energy*

The tip-leakage vortex, tip-leakage jet, and blade boundary layer separation generate strong turbulent kinetic energy. The governing equation for turbulent kinetic energy k is written as

$$\frac{Dk}{Dt} = \wp + T + \varepsilon, \tag{3.2}$$

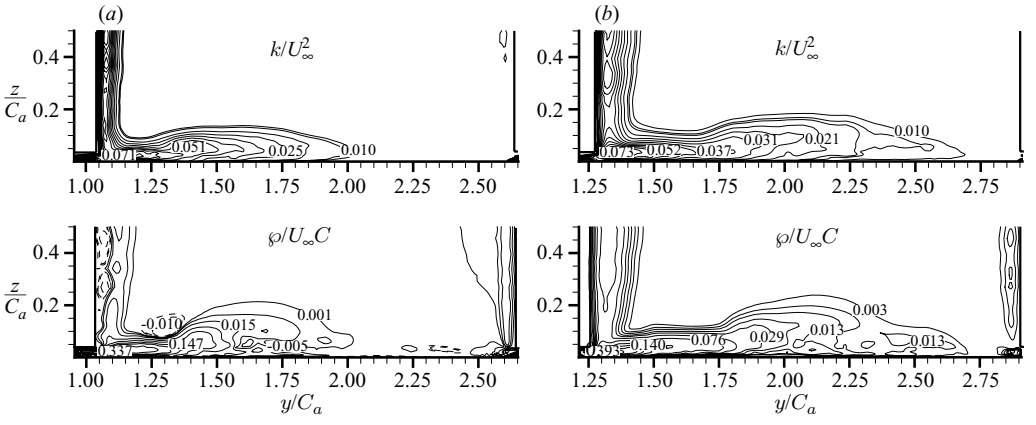

FIGURE 22. Contour plots of mean turbulent kinetic energy and turbulent-kinetic-energy production in (3.2) in y–z planes. (*a*) $x/C_a = 0.5$; (*b*) $x/C_a = 0.7$.

where

$$k = \frac{1}{2}\overline{u_i' u_i'}, \qquad \wp = -\overline{u_i' u_j'}\frac{\partial U_i}{\partial x_j},$$
$$T = -\frac{\partial}{\partial x_j}\left(\overline{u_j' p'} + \frac{1}{2}\overline{u_i' u_i' u_j'} - \frac{2}{Re}\overline{u_i' S_{ij}'}\right),$$
$$\varepsilon = -\frac{2}{Re}\overline{S_{ij}' S_{ij}'}, \qquad S_{ij}' = \frac{1}{2}\left(\frac{\partial u_i'}{\partial x_j} + \frac{\partial u_j'}{\partial x_i}\right).$$

Understanding the mechanism for turbulent-kinetic-energy production in the tip-leakage flow will shed light on the mechanisms for viscous losses by turbulent mixing in the cascade endwall region

Figures 22(*a*) and 22(*b*) show contour plots of mean turbulent kinetic energy (k/U_∞^2) and kinetic-energy production ($\wp/U_\infty C$) in y–z planes at two streamwise locations ($x/C_a = 0.5$ and 0.7). The gross shape of the turbulent-kinetic-energy distribution is similar to those found in the mean streamwise velocity and Reynolds normal-stress contour plots (figures 18 and 20). The tip-leakage vortex, tip-leakage jet, and blade boundary layer are the main sources of active turbulent kinetic energy. More precisely, the turbulent kinetic energy found in the tip-leakage jet and blade boundary layer is slightly higher than that in the tip-leakage vortex. High levels of turbulent kinetic energy in the tip-leakage jet and blade boundary layer region are consistently observed throughout the blade passage, while the magnitude of turbulent kinetic energy in the cross-stream measurement plane decreases along the axial direction.

A similar distribution shape is also observed in the contours of the turbulent-kinetic-energy production ($\wp$, figure 22). The endwall region is quite active in producing the turbulent kinetic energy. To examine the turbulent-kinetic-energy production in more detail, each term in $\wp$ (3.2) is considered separately. The production term is decomposed as:

$$\wp = \underbrace{-\overline{u'u'}\frac{\partial U}{\partial x}}_{\approx 0} \quad \underbrace{-\overline{v'v'}\frac{\partial V}{\partial y}}_{\wp_1} \quad \underbrace{-\overline{w'w'}\frac{\partial W}{\partial z}}_{\wp_2}$$

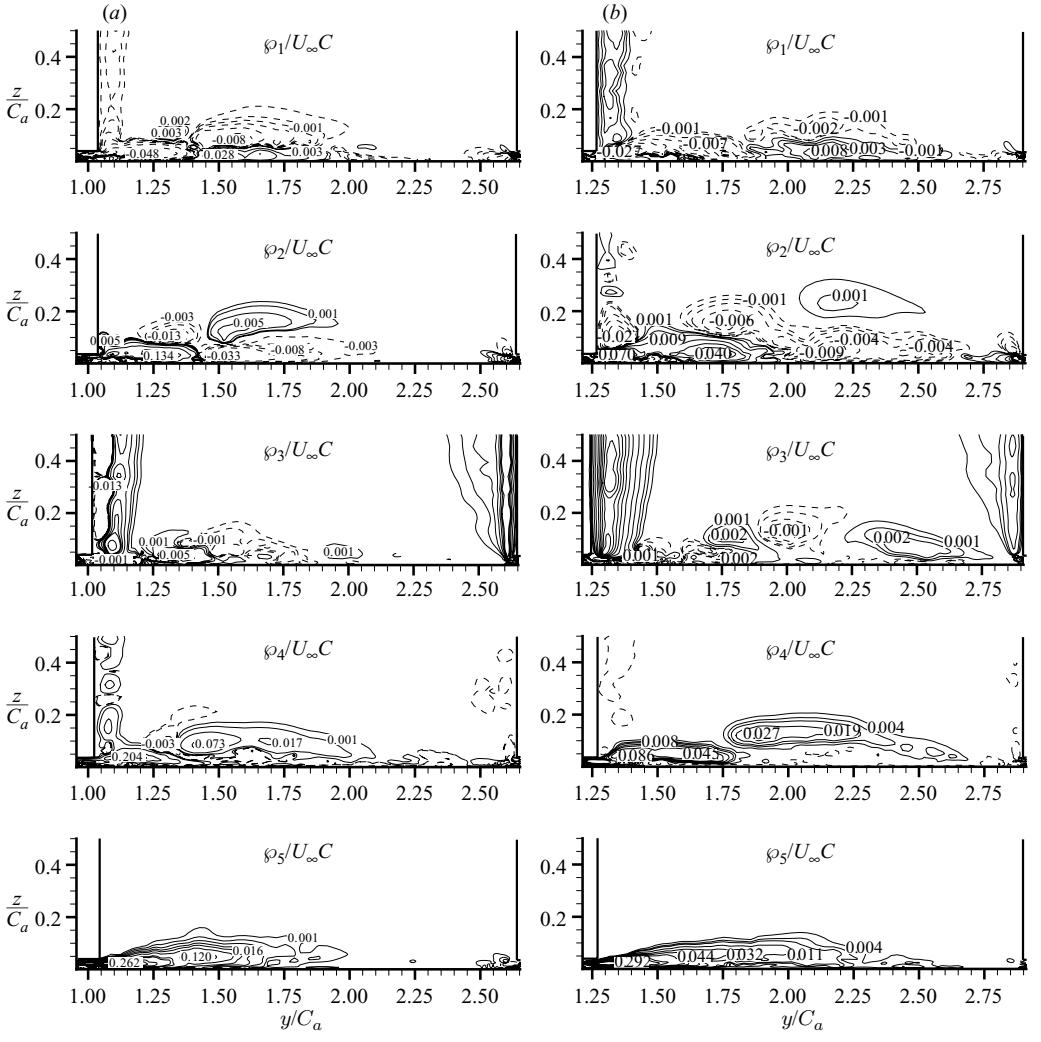

FIGURE 23. Contour plots of turbulent-kinetic-energy production components in (3.3) in y–z planes. (a) $x/C_a = 0.5$; (b) $x/C_a = 0.7$.

$$\underbrace{-\overline{u'v'}\left(\frac{\partial U}{\partial y}+\frac{\partial V}{\partial x}\right)}_{\wp_3}$$
$$\underbrace{-\overline{u'w'}\left(\frac{\partial U}{\partial z}+\frac{\partial W}{\partial x}\right)}_{\wp_4}$$
$$\underbrace{-\overline{v'w'}\left(\frac{\partial V}{\partial z}+\frac{\partial W}{\partial y}\right)}_{\wp_5}. \tag{3.3}$$

Since the production term $-\overline{u'u'}(\partial U/\partial x)$ becomes negligible, only the remaining 5 terms are considered in figures 23(a) and 23(b) in y–z planes at two streamwise locations ($x/C_a = 0.5$ and 0.7).

In the cascade passage, the turbulent-kinetic-energy production near the endwall is dominated by the $\wp_4$ and $\wp_5$ terms. Considering that the magnitudes of Reynolds shear-stress components are much smaller than those of Reynolds normal-stress components (figures 20*a* and 20*b*), it is evident that the spanwise derivatives of the mean streamwise and pitchwise velocity components are major sources of turbulent-kinetic-energy production. The $\wp_3$ term is found to dominate the turbulent-kinetic-energy production on the blade suction surface due to the pitchwise derivative of the streamwise velocity. The $\wp_1$ and $\wp_2$ terms are divided into four quadrants by their signs around the tip-leakage-vortex core, and their quadrants are in opposite phase to each other.

Throughout the blade passage, the tip-leakage jet produces the most significant levels of turbulent-kinetic-energy production (figure 20). This is due to the large spanwise derivatives of the streamwise or pitchwise velocity component caused by the rapid change of flow direction across the tip gap (see figure 17). Therefore, from these observations it is conclusive that significant turbulent kinetic energy is produced mainly by the streamwise and pitchwise velocity deficits in the tip-leakage flow. Muthanna & Devenport (2004) and Wang & Devenport (2004) also reported that most of the turbulence is generated by the axial deficit of the tip-leakage vortex rather than its rotating motion in the far downstream locations from the trailing edge.

4. Conclusions

An extensive analysis of the tip-clearance flow in a linear cascade with a moving endwall has been performed with an emphasis on understanding the mean flow field, turbulence characteristics, and vortex structures in the vicinity and downstream of the tip gap. The tip-leakage vortex is found to be the dominant vortical structure in the endwall region. It originates on the suction side of the blade tip at about 20 % to 30 % axial chord downstream from the leading edge. The trajectory of the tip-leakage vortex in the cascade passage is strongly affected by the moving endwall while it is mostly influenced by the cascade main stream after passing the trailing edge, where the core of the tip-leakage vortex is lifted from the endwall. The evolution of the tip-separation vortices, which are noticeable downstream from the blade tip near the trailing edge, is also significantly affected by the endwall motion because of their proximity to the endwall.

In addition, the endwall vortical structures, including the tip-leakage vortex, are well identified by significantly reduced streamwise velocity and by the sign changes in the cross-stream velocity components indicating circulating motions. As the tip-leakage vortex convects downstream, it is observed that the magnitudes of streamwise velocity in the cascade passage and the pitchwise velocity near the endwall are rapidly reduced. By this mechanism, the static pressure downstream of the cascade increases. The magnitude of the spanwise velocity is significantly smaller than those of the streamwise and pitchwise velocity components.

The tip-leakage vortex is also identified by the region of high streamwise and pitchwise vorticity magnitudes which suggest a helical configuration. The peak vorticity magnitude in the tip-leakage vortex is observed to decay as it develops downstream. The endwall region between the blade tip and the tip-leakage vortex produces higher vorticity levels in the streamwise and pitchwise components compared to those in the tip-leakage vortex. This is closely related to the direction of the tip-leakage jet which is generated by the pressure difference between the pressure and suction sides of the blade tip. The tip-leakage jet and tip-leakage vortex are found to produce significant spanwise and pitchwise derivatives of the streamwise and

pitchwise velocity components which result in highly enhanced vorticity magnitude. The tip-leakage vortex and tip-leakage jet are found to generate most of the Reynolds stresses and turbulent kinetic energy in the endwall region. This is also due to the large spanwise derivatives of the streamwise or pitchwise velocity components in the tip-leakage jet.

The peak deficit and turbulent fluctuations are found to drop rapidly as the tip-leakage vortex convects downstream. In the cascade passage, $\overline{u'u'}$ dominates the Reynolds stresses, while the three Reynolds normal-stress components are of comparable magnitude at downstream locations from the trailing edge. In general, Reynolds normal-stress components are found to attain higher magnitudes than Reynolds shear-stress components throughout the cascade. The strong influence of the tip-leakage jet on the production of vorticity and turbulent kinetic energy have been, surprisingly, less clearly identified in previous studies. This may be due to the difficulty in measuring the strong tip-leakage jet very close to the moving endwall using conventional experimental techniques and due to limitations of the RANS-based numerical approaches, which usually predict the mean flow field.

Furthermore, the above analysis suggests that the viscous loss due to the tip-leakage jet can be alleviated by changing the direction of the tip-leakage jet such that the associated spanwise and pitchwise derivatives of the mean velocity are reduced. Modifications of the blade profile and blade tip may be a feasible way of achieving this. For instance, one may employ a rib-like structure to channel the leakage jet towards a desirable direction. As mentioned in § 3.3.2, a vortex generator which generates vortices rotating in a direction opposite to that of the tip-leakage vortex can also be utilized to diminish its strength.

The authors acknowledge the support of the Office of Naval Research under Grant No. N00014-99-1-0389, with Dr Ki-Han Kim as the program manager. Computer time was provided by a Challenge Project Grant (C82) from the US Department of Defense (DoD) High Performance Computing Modernization Program (HPCMP) through Army Research Laboratory (ARL) and Aeronautical Systems Center (ASC) Major Shared Resource Centers (MSRC). The authors would also like to thank Professor William Devenport of VPI for providing his experimental data.

REFERENCES

Akselvoll, K. & Moin, P. 1995 Large eddy simulation of turbulent confined coannular jets and turbulent flow over a backward facing step. *Rep.* TF-63. Department of Mechanical Engineering, Stanford University, Stanford, California.

Ameri, A. A., Steinthorsson, E. & Rigby, D. L. 1999 Effects of tip clearance and casing recess on heat transfer and stage efficiency in axial turbines. *J. Turbomachinery* **121**, 683–693.

Bindon, J. P. 1989 Measurement and formation of tip clearance loss. *J. Turbomachinery* **111**, 257–263.

Fadlun, E. A., Verzicco, R., Orlandi, P. & Mohd-Yusof, J. 2000 Combined immersed-boundary finite-difference methods for three-dimensional complex flow simulations. *J. Comput. Phys.* **161**, 35–60.

Foley, A. C. & Ivey, P. C. 1996 3D laser transit measurements of the tip clearance vortex in a compressor rotor blade row. *ASME Paper* 96-GT-506.

Furukawa, M., Saiki, K., Nagayoshi, K., Kuroumaru, M. & Inoue, M. 1998 Effects of stream surface inclination on tip leakage flow fields in compressor rotors. *J. Turbomachinery* **120**, 683–692.

Goto, A. 1992 Three-dimensional flow and mixing in an axial flow compressor with different rotor tip clearance. *J. Turbomachinery* **114**, 675–685.

Hoeger, M., Fritsch, G. & Bauer, D. 1999 Numerical simulation of the shock-tip leakage vortex interaction in a HPC front stage. *J. Turbomachinery* **121**, 456–468.

Inoue, M., Kuroumaru, M. & Fukuhara, M. 1986 Behavior of tip-leakage flow behind an axial compressor rotor. *J. Engng Gas Turbines Power* **108**, 7–14.

Jeong, J. & Hussain, F. 1995 On the identification of a vortex. *J. Fluid Mech.* **285**, 69–94.

Kang, S. & Hirsch, C. 1993*a* Experimental study on the three-dimensional flow within a compressor cascade with tip clearance: part I-velocity and pressure fields. *J. Turbomachinery* **115**, 435–443.

Kang, S. & Hirsch, C. 1993*b* Experimental study on the three-dimensional flow within a compressor cascade with tip clearance: part II-the tip leakage vortex. *J. Turbomachinery* **115**, 444–452.

Kang, S. & Hirsch, C. 1994 Tip leakage flow in linear compressor cascade. *J. Turbomachinery* **116**, 657–664.

Khorrami, M. R., Li, F. & Choudhan, M. 2002 Novel approach for reducing rotor tip-clearance-induced noise in turbofan engines. *AIAA J.* **40**, 1518–1528.

Kuhl, D. D. 2001 Near wall investigation of three dimensional turbulent boundary layers. Master's thesis, Department of Aerospace and Ocean Engineering, Virginia Polytechnic Institute and State University, Blacksburg, Virginia.

Kunz, R. F., Lakshminarayana, B. & Basson, A. H. 1993 Investigation of tip clearance phenomena in an axial compressor cascade using Euler and Navier-Stokes procedures. *J. Turbomachinery* **115**, 453–467.

Lakshminarayana, B. 1996 *Fluid Dynamics and Heat Transfer of Turbomachinery*. John Wiley & Sons.

Lakshminarayana, B., Pouagare, M. & Davino, R. 1982 Three-dimensional flow-field in the tip region of a compressor rotor passage, part 1: mean velocity profiles and annulus wall boundary layer. *J. Engng Power* **104**, 760–771.

Lakshminarayana, B., Zaccaria, M. & Marathe, B. 1995 The structure of tip clearance flow in axial flow compressors. *J. Turbomachinery* **117**, 336–347.

Lund, T. S., Wu, X. & Squires, K. D. 1998 Generation of turbulent inflow data for spatially-developing boundary layer simulations. *J. Comput. Phys.* **140**, 233–258.

Ma, R. 2003 Unsteady turbulence interaction in a tip leakage flow downstream of a simulated axial compressor rotor. PhD thesis, Department of Aerospace and Ocean Engineering, Virginia Polytechnic Institute and State University, Blacksburg, Virginia.

Mailach, R., Lehmann, I. & Vogeler, K. 2001 Rotating instabilities in an axial compressor originating from the fluctuating blade tip vortex. *J. Turbomachinery* **123**, 453–460.

Meneveau, C., Lund, T. S. & Cabot, W. H. 1996 A Lagrangian dynamic subgrid-scale model of turbulence. *J. Fluid Mech.* **319**, 353–385.

Mittal, R. & Moin, P. 1997 Suitability of upwind-biased schemes for large-eddy simulation of turbulent flows. *AIAA J.* **36**, 1415–1417.

Muthanna, C. & Devenport, W. J. 2004 Wake of a compressor cascade with tip gap. Part 1. Mean flow and turbulence structure. *AIAA J.* **42**, 2320–2331.

Puddu, P. 1996 Tip leakage flow characteristics downstream of an axial flow fan. *ASME Paper* 96-GT-508.

de la Riva, D. H. 2001 Turbulence interaction in a highly staggered cascade-propulsor configuration. Master's thesis, Department of Aerospace and Ocean Engineering, Virginia Polytechnic Institute and State University, Blacksburg, Virginia.

Shin, S. 2001 Reynolds-averaged Navier-Stokes computation of tip-clearance flow in a compressor cascade using an unstructured grid. PhD thesis, Department of Aerospace and Ocean Engineering, Virginia Polytechnic Institute and State University, Blacksburg, Virginia.

Stauter, R. C. 1993 Measurements of the three-dimensional tip region flow field in an axial compressor. *J. Turbomachinery* **115**, 468–476.

Storer, J. A. & Cumpsty, N. A. 1990 Tip leakage flows in axial compressors. *ASME Paper* 90-GT-127.

Storer, J. A. & Cumpsty, N. A. 1994 Approximate analysis and prediction method for tip clearance loss in axial compressors. *J. Turbomachinery* **116**, 648–656.

Suder, K. L. 1998 Blockage development in a transonic, axial compressor rotor. *J. Turbomachinery* **120**, 465–476.

Wang, Y. & Devenport, W. J. 2004 Wake of a compressor cascade with tip gap. Part 2. Effects of endwall motion. *AIAA J.* **42**, 2332–2340.

Wenger, C. W., Devenport, W. J., Wittmer, K. S. & Muthanna, C. 2004 Wake of a compressor cascade with tip gap. Part 3. Two-point statistics. *AIAA J.* **42**, 2341–2346.

You, D., Mittal, R., Wang, M. & Moin, P. 2004*a* Computational methodology for large-eddy simulation of tip-clearance flows. *AIAA J.* **42**, 271–279.

You, D., Mittal, R., Wang, M. & Moin, P. 2006*a* Analysis of stability and accuracy of finite-difference schemes on a skewed mesh. *J. Comput. Phys.* **213**, 184–204.

You, D., Moin, P., Wang, M. & Mittal, R. 2004*b* Study of tip clearance flow in a turbomachinery cascade using large eddy simulation. *Rep.* TF-86. Department of Mechanical Engineering, Stanford University, Stanford, California.

You, D., Wang, M. & Moin, P. 2006*b* Large-eddy simulation of flow over a wall-mounted hump with separation control. *AIAA J.* **44**, 2571–2577.

You, D., Wang, M., Moin, P. & Mittal, R. 2005 Vortex dynamics and mechanisms for viscous losses in the tip-clearance flow. *ASME FEDSM* 2005-77175.

Zierke, W. C. & Straka, W. A. 1996 Flow visualization and the three-dimensional flow in an axial flow pump. *J. Propulsion Power* **12**, 250–259.